Title

Mechanical stress analysis of a rigid inclusion in distensible material: a model of atherosclerotic calcification and plaque vulnerability

Journal

AJP Heart and Circulatory Physiology, 297(2)

ISSN

0363-6135

Authors

Hoshino, Tetsuya
Chow, Lori A
Hsu, Jeffrey J
et al.

Publication Date

2009-08-01

DOI

10.1152/ajpheart.00318.2009

AMERICAN JOURNAL OF PHYSIOLOGY
HEART AND CIRCULATORY PHYSIOLOGY

Am J Physiol Heart Circ Physiol. 2009 Aug; 297(2): H802–H810.
Published online 2009 Jun 19. doi: 10.1152/ajpheart.00318.2009: 10.1152/ajpheart.00318.2009

PMCID: PMC2724207
PMID: 19542489

Mechanical stress analysis of a rigid inclusion in distensible material: a model of atherosclerotic calcification and plaque vulnerability

Tetsuya Hoshino,[1] Lori A. Chow,[2] Jeffrey J. Hsu,[3] Alice A. Perlowski,[3] Moeen Abedin,[3] Jonathan Tobis,[3] Yin Tintut,[3] Ajit K. Mal,[1,2] William S. Klug,[1,2] and Linda L. Demer[2,3,4]

Departments of [1]Mechanical and Aerospace Engineering, [2]Biomedical Engineering, [3]Medicine (Cardiology), and [4]Physiology, University of California, Los Angeles, California

Address for reprint requests and other correspondence: L. L. Demer, Division of Cardiology, The David Geffen School of Medicine at UCLA, 10833 LeConte Ave., Box 951679, Los Angeles, CA 90095-1679 (e-mail: ldemer@mednet.ucla.edu)

Received 2009 Apr 2; Accepted 2009 Jun 15.

Abstract

The role of atherosclerotic calcification in plaque rupture remains controversial. In previous analyses using finite element model analysis, circumferential stress was reduced by the inclusion of a calcium deposit in a representative human anatomical configuration. However, a recent report, also using finite element analysis, suggests that microscopic calcium deposits increase plaque stress. We used mathematical models to predict the effects of rigid and liquid inclusions (modeling a calcium deposit and a lipid necrotic core, respectively) in a distensible material (artery wall) on mechanical failure under uniaxial and biaxial loading in a range of configurations. Without inclusions, stress levels were low and uniform. In the analytical model, peak stresses were elevated at the edges of a rigid inclusion. In the finite element model, peak stresses were elevated at the edges of both inclusions, with minimal sensitivity to the wall distensibility and the size and shape of the inclusion. Presence of both a rigid and a soft inclusion enlarged the region of increased wall stress compared with either alone. In some configurations, the rigid inclusion reduced peak stress at the edge of the soft inclusion but simultaneously increased peak stress at the edge of the rigid inclusion and increased the size of the region affected. These findings suggest that the presence of a calcium deposit creates local increases in failure stress, and, depending on relative position to any neighboring lipid pools, it may increase peak stress and the plaque area at risk of mechanical failure.

Keywords: plaque rupture, vulnerable plaque, atherosclerosis, vascular calcification

CALCIUM DEPOSITS, WHICH OCCUR commonly in atherosclerotic plaque, introduce mechanical discontinuities with compliance mismatch where they interface with the surrounding distensible tissue. Mechanical vulnerability is a central determinant of myocardial infarction and other acute coronary syndromes (14), and it has been shown to increase when the plaque has a lipid pool under a thin cap (23, 31). Some recent evidence points to calcium deposits as also playing a role in mechanical vulnerability. In balloon an-

gioplasty imaged dynamically by intravascular ultrasound, plaque failure is seen to occur along the edge of calcium deposits (15). On the basis of computed tomographic scanning of coronary arteries, the severity of calcification in coronary arteries correlates with cardiovascular events (1) at least as well as, and possibly better than, conventional risk factor analysis (28). Extensive histopathological analyses performed by investigators at the Armed Forces Institute of Pathology have suggested that calcification may contribute, in part, to human plaque rupture (6). On the basis of intravascular ultrasonic images, patients with stable angina have greater circumferential arcs of coronary calcification than patients with unstable angina (3). Also using intravascular ultrasound, Ehara et al. (12, 13) found that patients with stable angina have fewer, larger contiguous deposits, whereas patients with acute coronary syndromes have many more and smaller deposits, which they termed "spotty calcification." These findings support the concept that interfacial area of calcium deposits is a determinant of plaque stability (29).

Theoretical analyses also indicate complex effects of calcium deposits. Huang et al. (17) used finite element analysis of a two-dimensional model of plaque with both lipid and calcium deposits based on the geometry of 20 actual patients. Results predicted that calcium deposits reduce maximal circumferential stress. Similarly, Imoto et al. (19), using the concept of "equivalent stress" in both idealized and realistic models of plaque, found that superficial calcification reduced surface stress in a fibrous cap, whereas calcium deposits at the abluminal side of a plaque had little or no effect on the level of surface equivalent stress. However, a mathematical model of a thin fibrous cap with microscopic calcium deposits predicted that 10-μm-diameter rigid inclusions nearly double the circumferential stress (35). Thus the predicted effects of calcium deposits vary even among theoretical analyses.

An important determinant of the mechanical consequences of calcium deposits on the plaque stability may be location within the vessel wall. Recent work by Li et al. (22) assessed the importance of the location of a calcified nodule on stress distribution within the atherosclerotic vessel wall. In their finite element model analysis, peak stresses were highly concentrated in the region immediately adjacent to the vessel wall, and changes in stress distribution were primarily found in this high-stress area. Their model predicts that calcification within a thin fibrous cap can increase peak stress in the cap by ~50%, whereas calcification in regions more distant from the lumen have no significant effect on peak stress. However, rupture is not limited to regions experiencing maximal stress, probably because of regional variation in mechanical strength; multiple groups have used computational models to demonstrate that plaque rupture may occur in regions that are not predicted to experience the highest stress (7, 32). The presence of calcified deposits, even if distant from the region experiencing maximal circumferential stress, may introduce local peak stresses on regions of the vessel wall that are less capable of handling them. The local environment of these deposits, which commonly includes neighboring lipid pools, may contribute significantly to the stress distribution that results from the presence of calcification.

In this study, we hypothesized that macroscopic calcium deposits introduce local elevations in peak stress at their edges as do microscopic deposits and that effects on neighboring lipid deposits depend on their proximity and respective distances from the lumen. We used analytical and numerical analyses to theoretically determine the peak stresses (maximal principal and von Mises stresses) and their distributions during loading of a basic, generalizable model of an elastic artery with round calcific (rigid) and/or lipidic (soft) inclusions. Rather than using a single example of plaque geometry, we allowed geometric parameters, such as location of deposits relative to lumen and to one another, to vary over physiological ranges, allowing greater generalization of findings. This characterization of the effects of plaque composition and geometry on the stress distribution in an atherosclerotic lesion may allow for more accurate identification of vulnerable plaques.

METHODS

The physical problem is that of a deformable vessel, under distending pressure, with a rectilinear axis and a circular cross section containing a rigid inclusion, a soft inclusion, or both, with variable proximity to one another and to the vessel lumen.

Analytical model. For the analytical model, we considered a rectangular domain of the vessel wall topologically approximated by a thin, flat, rectangular membrane, representing a circumferential slice of the vessel, under uniaxial or biaxial tension, as would be generated by arterial blood pressure (Fig. 1). The calcium deposit was modeled as a circular inclusion of rigid material of equal thickness to and fused to the distensible material subject to remote stresses.

The stresses at the interface between the rigid circular inclusion and the vessel wall were calculated by standard techniques (25). For a rigid inclusion, the polar components of the stress at a general point (r, θ) (Fig. 1) are expressed in the form

$$\sigma_{ij}(r,\ \theta) = \sigma_x^0 f_{ij}(\mathrm{r},\ \theta) + \sigma_y^0 f_{ij}(r,\ \theta - 90^\circ) \tag{1}$$

where the indices i and j are either r or θ, σ_x^o and σ_y^o are the remote applied stresses, and the functions f_{ij} are given by

$$f_{rr} = \frac{1}{2}\left\{1 + \alpha\frac{a^2}{r^2} + \left[1 + 4\beta\frac{a^2}{r^2} - 3\beta\frac{a^4}{r^4}\right]\cos 2\theta\right\}$$

$$f_{\theta\theta} = \frac{1}{2}\left\{1 - \alpha\frac{a^2}{r^2} - \left[1 - 3\beta\frac{a^4}{r^4}\right]\cos 2\theta\right\} \tag{2}$$

$$f_{r\theta} = -\frac{1}{2}\left[1 - 2\beta\frac{a^2}{r^2} + 3\beta\frac{a^4}{r^4}\right]\sin 2\theta$$

The parameters α and β are related to the Poisson's ratio, ν, of the vessel material through

$$\alpha = \frac{1-\nu}{1+\nu},\ \beta = \frac{1+\nu}{3-\nu} \tag{3}$$

The Poisson's ratio is constant for a particular material. When a material is stretched in a given dimension, the other two dimensions contract passively. The Poisson's ratio is the ratio of the contraction vs. the stretch. For a perfectly incompressible material, this ratio is 0.5. On the basis of values for vascular

tissue in the literature, the Poisson's ratio, ν, was initially assumed to be 0.45. However, to allow for variable properties and to assess the robustness of the model-based results, we repeated the simulation for values of Poisson's ratio ranging from 0.25 to 0.49.

Failure analysis was carried out in a technical computing environment, MATLAB (MathWorks, 2001), using the maximum principal stress theory or von Mises theory (34). The maximum principal stress theory of failure assumes that the material fails when the maximum principal stress, σ_{max}, exceeds a failure threshold, σ_F, characteristic of that material, where

$$\sigma_{max} = \frac{1}{2}\mathrm{Max}\left\{(\sigma_\pi + \sigma_{\theta\theta}) \pm \sqrt{(\sigma_\pi - \sigma_{\theta\theta})^2 4\sigma_{\Gamma\theta}^2}\right\} \quad (4a)$$

The von Mises theory provides a failure criterion for ductile materials and indicates that failure occurs when, at any point in the body, the distortion energy per unit volume in a state of combined stress becomes equal to that associated with failure under a uniaxial tension test; this allows for prediction of mechanical failure based on the level of von Mises stress, which is a combined term calculated from the stresses acting in each of the principal axes as well as shear stress terms. Thus failure occurs if $\sigma_V \geq \sigma_F$, where the von Mises stress, σ_V, is related to the stress components through the equation

$$\sigma_v = (\sigma_\pi^2 + \sigma_{\theta\theta}^2 - \sigma_\pi\sigma_{\theta\theta} + 3\sigma_{\Gamma\theta}^2)^{1/2} \quad (4b)$$

The von Mises stress was calculated to show the sites of expected failure based on assessing failure criteria at each point in models with and without the rigid inclusion. The stresses were determined relative to the applied stress, σ_0, which was taken to be 1.0 arbitrary units.

For the biaxial loading case, stress was applied along the *x*-axis (longitudinal) and the *y*-axis (circumferential). In a closed-ended, thin-walled cylindrical vessel under internal pressure, the circumferential (σ_C) and longitudinal (σ_L) stresses are $(pR_m)/(t)$ and $(pR_m)/(2t)$, respectively, where p is internal pressure, R_m is the mean radius, and t is the vessel thickness. Thus, for the biaxial case, the longitudinal stress can be estimated as half of the applied circumferential stress.

The rigid inclusion was given a radius of 1.0 arbitrary unit centered at coordinates (0, 0). Stresses were analyzed in the entire domain, from the inclusion-vessel interface (r = 1) to the edge of the local domain (r = 4). The radial and angular positions were varied, and stresses were determined for each position. Data were generated for polar plots of radial (σ_{rr}), circumferential ($\sigma_{\theta\theta}$), shear ($\sigma_{r\theta}$), normalized maximum principal (σ_{max}), and von Mises (σ_V) stresses for a membrane with and without a planar, circular, rigid inclusion and compared on the same scale.

Finite element model. The analytical model described above idealizes the vessel wall as a thin solid, focusing on the distribution of stress in the plane tangent to the vessel boundary. To study the effects of lipid and mineral geometry on stress distributions through the thickness of the vessel, a finite element model was built of an arterial cross section. Consistent with previous studies (17) deformation along the vessel axis was neglected through the adoption of a two-dimensional plane-strain framework. As shown schematically in Fig. 2, a portion of the vessel wall is modeled as an elastic strip under an applied circumferential tension of circumferential tension (τ) of 10 kPa produced by arterial blood pressure. Within the vessel wall were placed a soft inclusion modeling a lipid core and a hard inclusion modeling a mineral de-

posit. The relative size, separation, and orientation of the two inclusions were varied over a wide range, as shown in the schematic, and the deformations and resulting stress distributions were computed with the finite element analysis software package ABAQUS (ABAQUS/Standard; DS Simulia, Providence, RI).

Following Huang et al. (17), the nonlinear elastic constitutive behavior of the vessel wall, the lipid inclusion, and the mineral inclusion were described via an incompressible hyperelastic strain energy model. In particular, Huang et al. made use of the strain-energy function (W) suggested by Delfino et al. (10),

$$W = \frac{a}{b}\left\{\exp\left[\frac{b}{2}(I_1 - 3)\right] - 1\right\}$$

, where I_1 is the first invariant (i.e., the trace) of the right Cauchy-Green deformation tensor and $\alpha = 44.2$ kPa and $\beta = 16.7$ are constants determined experimentally for an artery wall (9). The properties of the mineral and lipid inclusions are taken from Huang et al.

In the present work, a three-term Taylor-expanded approximation of this model was employed with use of the Yeoh form available in ABAQUS

$$W = \frac{a}{2}(I_1 - 3) + \frac{ab}{8}(I_1 - 3)^2 + \frac{ab^2}{48}(I_1 - 3)^3.$$

The top and bottom boundaries of the vessel were assigned traction-free boundary conditions, and the entire assembly was meshed with eight-node quadrilateral finite elements. The mesh density (number of elements) was iteratively refined until convergence of peak stresses was attained.

Parameter studies were performed, computing deformations of the vessel wall and the corresponding stress distributions for various combinations of the parameters (Fig. 2) determining the geometry of the inclusions: relative size, separation distance, and relative orientation.

Biological models. For in vitro analysis, calcifying vascular cells (CVC), a subpopulation of purified bovine aortic medial smooth muscle cells, were cultured as described previously (33). Briefly, CVC were grown in Dulbecco's modified Eagle's medium (Invitrogen) containing 15% fetal bovine serum (HyClone) for 30 days with fresh media added every 3–4 days. In culture, CVC spontaneously form discrete, three-dimensional, mineralized nodules arising from a cellular monolayer (33). After 30 days, ascorbic acid (50 μg/ml) was used to detach the culture intact from the plastic dish. The cell layer, including mineralized nodules, was transferred to a strip of parafilm, which was subjected to gradually increasing uniaxial stress until cell layer rupture.

As an ex vivo model, *ldlr*$^{(-/-)}$ mice were placed on a Western diet (Teklad no. TD90221) for 2 mo. At the end of the diet, corresponding to 4 mo of age, the mice were euthanized. The pericardium was opened and the ascending aortas were separated from mediastinal attachments, leaving intact attachments to the great vessels, descending aorta, and heart. Uniaxial stretch was applied by gradually increasing caudal displacement of the heart until vessel rupture. After rupture, the ascending aorta was removed, mounted and stained with Oil Red O. All experiments were conducted in accordance with the protocols approved by the UCLA Institutional Review Board and the UCLA Animal Research Committee.

Additionally, to assess the effect of increased circumferential stress on human calcified atherosclerotic plaque ex vivo, human coronary arteries obtained from autopsy were subjected to intraluminal balloon inflation (PowerSail RX, 4.0 mm; Abbott Laboratories). Cross sections of the specimens were visualized before and after balloon inflation by intravascular ultrasound (IVUS; Galaxy, Boston Scientific), with an Atlantis SR Pro catheter (Boston Scientific). IVUS images were processed with OsiriX Imaging Software.

RESULTS

Analytical model. Computational analysis using this model showed that, under uniaxial loading, radial stress was increased by addition of the rigid inclusion (Fig. 3*A*), with the greatest increase (~40%) at the ends of the deposit facing the loading axis. Circumferential stress was slightly decreased by the rigid inclusion (Fig. 3*B*) particularly along the edges perpendicular to the loading axis, consistent, although not directly comparable, with the findings of Huang et al. (17). Shear stress was similar with and without the inclusion (Fig. 3*C*). Both indicators of failure stress, the maximum principal and the von Mises stresses, were increased by the inclusion, with highest concentration at the edges of the deposit facing the loading axis (Fig. 3, *D* and *E*). Importantly, in the absence of the deposit, normalized maximum principal stress and von Mises stress were low and distributed uniformly without sites of concentration (Fig. 3, *D* and *E*).

Under biaxial loading, radial stresses were distributed more widely, but the pattern of all stresses was similar. Stress distribution and degree also changed with inclusion of the rigid deposit in a manner similar to that in the uniaxial case (Fig. 4). As with uniaxial loading, radial stress was increased with the rigid deposit (Fig. 4*A*). Circumferential stress was slightly decreased at the edges perpendicular to the axis of greater loading (Fig. 4*B*). Shear stress was lower with biaxial vs. uniaxial loading in the presence or absence of the deposit. Shear stress magnitude was minimally affected by the deposit (Fig. 4*C*). Both indicators of failure stress were greater in the presence of the rigid deposit, and they were concentrated at the ends of the deposit facing the axis of greater load (Fig. 4, *D* and *E*). These failure stresses were ~20% greater with biaxial vs. uniaxial loading.

In general, radial stress, normalized maximum principal stress, and von Mises stress were greater than circumferential and shear stress (Fig. 3). Radial stress exhibited the greatest dependency on theta (Figs. 3*A* and 4*A*). Radial stress was maximal in the direction of the loading axis, circumferential stresses were maximal perpendicular to the load axis, and shear stresses were maximal at 45° from the load axis (Figs. 3, *A*–*C* and 4, *A*–*C*) under both loading conditions.

The domain size of four arbitrary units (radii) was selected for ease of viewing the stress pattern. Beyond the image limits, stresses remain positive but diminish with distance from the inclusion. In the uniaxial stress model, radial, circumferential, and shear stresses were compared on one scale (0–1.25 σ_0), and the normalized maximum principal stress and von Mises stress were compared on another scale (0–1.5 σ_0), even though the highest values differ, to allow comparison without compromising the full scale. Similarly, in the biaxial stress model, radial, circumferential, and shear stresses are compared on one scale (0–1.4 σ_0) and the normalized maximum principal stress and von Mises stress are compared on another scale (0.8–1.4 σ_0).

Because the Poisson's ratio of the material may vary with the type of atherosclerotic plaque and degree of fibrosis, stress was recalculated for a range of values of Poisson's ratio (from 0.25 to 0.49) at several representative locations in the domain, including points at 1.1 and 2.5 radii from the origin at theta angles of 0°, 45°, 90°, 135°, and 180°. At all values of Poisson's ratio, the failure stress remained greater in the presence of the rigid inclusion and remained concentrated at the same edges of the deposit. In both

the presence and absence of the rigid deposit and in the uniaxial and biaxial cases, at the position defined by r = 1.1 and θ = 0°, radial stress, maximum principal stress, and von Mises stress decreased slightly as Poisson's ratio was increased, whereas circumferential and shear stresses increased slightly. Similarly, for θ = 90° at the same radial position, the radial stress and normalized maximum principal stress decreased whereas von Mises and shear stress increased with increasing Poisson's ratio. Interestingly, circumferential stress increased slightly with Poisson's ratio in the biaxial model but tended to decrease slightly in the uniaxial model irrespective of the presence of the deposit. Importantly, the finding of increased von Mises stress in the presence of a rigid inclusion for both uniaxial and biaxial load models was not affected by changes in the value of Poisson's ratio.

Finite element model. Parametric studies using the finite element model described above showed that varying both the sizes of and the separation distance between the mineral and lipid inclusions led to minimal change in the peak values and distributions of the resulting stresses. Similarly stresses are insensitive to variations in the shape of inclusions (data not shown), provided that their boundaries are smooth (sharp features can produce local concentrations of stress). Analysis of the model showed that the most striking changes in stress patterns are linked to variation of the orientation of the pair of inclusions, as represented by the angle θ between the center-to-center axis and horizontal (see Fig. 2). This is demonstrated in Fig. 5, which shows plots of the von Mises stress calculated for a lipid inclusion alone (Fig. 5*A*) and for mineral and lipid inclusions in three different orientations: θ = 0° (Fig. 5*B*), θ = 45° (Fig. 5*C*), and θ = 90° (Fig. 5*D*).

From Fig. 5, it is clear that in all cases the peak stresses occur in regions of the tissue closest to the top and bottom edges of the lipid inclusion. This is understandable, because the weakened load-bearing capacity of the softer neighboring lipid material will cause additional stress to be "channeled" into the surrounding tissue. This same pattern is observed even with a lipid inclusion in the absence of any mineral inclusion (Fig. 5*A*), in which case the maximum von Mises stress above and below the lipid inclusion is 88 kPa. As is evident from the legends of Fig. 5, *B*–*D*, addition of the mineral inclusion can produce peak stresses that are sometimes larger and sometimes smaller than for the lipid alone: whereas mineral inclusions at θ = 0° and θ = 45° reduce the peak stresses at the edge of the rigid deposit, the inclusion at θ = 90° increases the peak stress at that edge. These results suggest a variable role of calcium deposits in stabilizing (or destabilizing) arterial plaques. Furthermore, beyond the simple comparison of peak stresses, analysis of the results reveals that the location of the rigid inclusion has a pronounced effect on the distribution of stresses in the tissue surrounding the lipid inclusion. Namely, in the cases of θ = 0° and θ = 45°, the reduction of peak stresses at the edge of the rigid deposit appears to occur because of a redistribution of stress into a larger region of surrounding tissue. This is evidenced by the increased area of green pseudocolor in Fig. 5, *C* and *D*, where the stresses are at least twice the magnitude of the applied tension. Figure 5*E* shows a close-up view of this region of elevated stress from Fig. 5*D*.

Biological models. To test whether the site of failure predicted by the model corresponds with actual rupture sites biologically, we tested three models of vascular calcification: calcified nodules in vascular cell culture, mouse aortic calcification, and human coronary calcification. In the in vitro culture model, uniaxial loading produced failure at the edge of a calcified nodule facing the direction of applied stress (Fig. 6*A*), as predicted by the analytical model. Similarly, in the ex vivo mouse model of calcific atherosclerosis, uniaxial loading of the ascending aorta produced a full-thickness tear at the edge of an aortic calcium deposit facing the direction of applied stress (Fig. 6*B*), as predicted by the analytical model. Lastly, in the ex vivo samples of human coronary calcification, circumferential stress applied by intraluminal balloon inflation induced full-thickness rupture at the interface between a calcium deposit and adjacent soft tissue (Fig. 6, *C* and *D*), also as predicted. The geometry of the calcified deposit in this ex vivo model was found

to be similar to the geometry used in the analytical model (Fig. 1). It should be noted that the stress applied by the balloon is transmitted circumferentially to the vessel wall, and failure is seen to occur at the circumferential edge of the calcium deposit.

DISCUSSION

These theoretical analyses suggest that addition of a circular rigid deposit to a thin, flat distensible material under load introduces high local peak stress at its edges, independent of the magnitude of applied stress, the size of the inclusion, and the elastic properties of the distensible material. The lack of sensitivity to material properties is consistent with the results of Williamson et al. (37). Previous studies also showed that calcified arteries are less compliant (2, 11, 16, 26, 27, 30) and that they fail abruptly at lower tension than controls (11, 20, 30). This is further supported by the finding that mice with extensive aortic calcification due to matrix GLA protein deficiency almost uniformly die prematurely of aortic rupture (24).

Several studies have addressed the effects of calcification on the stability of atherosclerotic plaques by calculating changes in global maximal stress (17, 22, 32, 35). However, mechanical failure is determined by the balance of mechanical stress vs. material strength, with rupture occurring where stress exceeds strength. Thus global maximal stresses may be concentrated in strong, nondiseased regions in the vessel wall, and rupture has been shown to occur in regions not predicted to experience the highest stress (7, 32). As such, Tang et al. (32) have proposed a "local maximal stress hypothesis," in which they emphasize the importance of analyzing local maximal stresses in critical locations of atherosclerotic plaque. Using sections of human specimens of atherosclerotic vessels to design their finite element model, they predicted local maximal stresses on the order of 60 kPa in critical areas. In our finite element analysis, stress near calcium deposits was of the same order of magnitude; however, the actual peak stress immediately adjacent to the rigid deposit would be underestimated owing to the partial volume effect of mesh elements, with greater underestimation with larger mesh size. Cheng et al. (7) previously estimated that plaque rupture requires a global maximal stress of 300 kPa, on the basis of analysis of human plaque rupture, primarily at the fibrous cap. Since strength is expected to be higher in the fibrous cap, the stress required for rupture would be higher there. In deeper areas of plaque, where macroscopic calcium deposits tend to occur, the strength, and hence the threshold for intraplaque rupture, may be lower than in the fibrous cap. Thus the present analysis focuses on macroscopic calcium deposits located at varying depths and at varying orientations relative to the lumen and adjacent lipid deposits, distinguishing it from prior analyses focused on specific human anatomy and on microscopic deposits within the fibrous cap. This analysis provides the novel information that, whereas large calcium deposits may reduce the maximum stress at the edges of adjacent lipid deposits, they increase the area affected by failure stress, especially when located at greater depths in the artery wall.

Ectopic calcification within the vessel wall has long been known to share developmental features with bone formation, a key element of which is the invasion of heavily vascularized young connective tissue into calcified tissue (4, 5). More recent work has addressed the mechanisms involved in the neovascularization of calcified atherosclerotic plaques, and Wilkinson et al. (36) have proposed a potential inhibitory role for vascular calcification associated factor. The presence of fragile neovessels in the tissue surrounding a calcium deposit would result in *1*) a lower threshold for rupture of that tissue and *2*) a greater likelihood of intraplaque hemorrhage, which is a common cause of myocardial infarction. This could explain the intriguing finding of Davies et al. (8) that myocardial infarction in the absence of intracoronary

thrombus was almost always associated with severe coronary calcification of the culprit artery. Intraplaque hemorrhage also contributes to the destabilization of plaques and the progression to plaque rupture (21).

The models in this study have certain limitations. In the computational models, the deposits were idealized as circular, which is reasonable given the lack of any one typical or representative geometry for atherosclerotic calcium deposits and the lack of sensitivity of the results to the shape of the deposits (data not shown). Another limitation is that the distensible material surrounding the deposits, representing either atherosclerotic plaque or normal artery wall, was assumed to be homogeneous and isotropic, although plaque is heterogeneous and normal artery wall is anisotropic (18). Incorporating anisotropy and/or deposits of different shapes in the model are expected to alter only details of the distribution of the increase in peak stresses but not the overall conclusions. Since values for fluid shear stress in small arteries (~1 Pa) are orders of magnitude less than those calculated in this study (>10,000 Pa), effects of fluid shear stress at the lumen are expected to be minimal and thereby were not incorporated. In the biological models, the applied tension was not mechanized or quantified; however, the analysis predicts the results to be independent of rate and amplitude of the applied tension.

These findings suggest that addition of a rigid deposit to a distensible material under stress may increase or decrease risk of mechanical failure at different locations in the material, depending on proximity and orientation of the rigid deposit relative to a liquid inclusion. By bearing load, a rigid deposit decreases peak stress in some areas. By introducing compliance mismatch, it increases peak stress at other sites. Thus atherosclerotic calcification is expected to have complex effects on plaque vulnerability, with failure risk increased at some sites and decreased at others and with dependence on location and orientation relative to lipid deposits.

GRANTS

This research was funded in part by National Institutes of Health Grants HL69261 and DK081346, American Heart Association Grant GIA 0555028Y, UCLA Graduate Opportunity Fellowship Award (L. A. Chow), a grant from the UCLA Academic Senate, and the Howard Hughes Medical Institute Research Training Fellowship (J. J. Hsu).

Acknowledgments

We would like to thank Dr. Jinxiu Lu for technical assistance with the histological experiments.

Present address for M. Abedin: Cardiovascular Section, University of Oklahoma, P.O. Box 26901, WP3010, Oklahoma City, OK 73190.

REFERENCES

1. Arad Y, Spadaro LA, Roth M, Scordo J, Goodman K, Sherman S, Lledo A, Lerner G, Guerci AD. Correlations between vascular calcification and atherosclerosis: a comparative electron beam CT study of the coronary and carotid arteries. *J Comput Assist Tomogr* 22: 207–211, 1998. [PubMed: 9530380]

2. Band W, Goedhard WJ, Knoop AA. Comparison of effects of high cholesterol intake on viscoelastic properties of the thoracic aorta in rats and rabbits. *Atherosclerosis* 18: 163–171, 1973. [PubMed: 4741532]

3. Beckman JA, Ganz J, Creager MA, Ganz P, Kinlay S. Relationship of clinical presentation and calcification of culprit coronary artery stenoses. *Arterioscler Thromb Vasc Biol* 21: 1618–1622, 2001. [PubMed: 11597935]

4. Buerger L, Oppenheimer A. Bone formation in sclerotic arteries. *J Exp Med* 10: 354–367, 1908. [PMCID: PMC2124523] [PubMed: 19867136]

5. Bunting CH The formation of true bone with cellular (red) marrow in a sclerotic aorta. *J Exp Med* 8: 365–376, 1906. [PMCID: PMC2124622] [PubMed: 19867044]

6. Burke AP, Kolodgie FD, Farb A, Weber D, Virmani R. Morphological predictors of arterial remodeling in coronary atherosclerosis. *Circulation* 105: 297–303, 2002. [PubMed: 11804983]

7. Cheng GC, Loree HM, Kamm RD, Fishbein MC, Lee RT. Distribution of circumferential stress in ruptured and stable atherosclerotic lesions. A structural analysis with histopathological correlation. *Circulation* 87: 1179–1187, 1993. [PubMed: 8462145]

8. Davies MJ, Woolf N, Robertson WB. Pathology of acute myocardial infarction with particular reference to occlusive coronary thrombi. *Br Heart J* 38: 659–664, 1976. [PMCID: PMC483064] [PubMed: 973888]

9. Delfino A *Analysis of the stress field in a model of the human carotid bifurcation.* Lausanne, Switzerland: Federal Institute of Technology, 1996.

10. Delfino A, Stergiopulos N, Moore JE Jr, Meister JJ. Residual strain effects on the stress field in a thick wall finite element model of the human carotid bifurcation. *J Biomech* 30: 777–786, 1997. [PubMed: 9239562]

11. Demer LL Effect of calcification on in vivo mechanical response of rabbit arteries to balloon dilation. *Circulation* 83: 2083–2093, 1991. [PubMed: 2040058]

12. Ehara S, Kobayashi Y, Yoshiyama M, Shimada K, Shimada Y, Fukuda D, Nakamura Y, Yamashita H, Yamagishi H, Takeuchi K, Naruko T, Haze K, Becker AE, Yoshikawa J, Ueda M. Spotty calcification typifies the culprit plaque in patients with acute myocardial infarction: an intravascular ultrasound study. *Circulation* 110: 3424–3429, 2004. [PubMed: 15557374]

13. Ehara S, Kobayashi Y, Yoshiyama M, Ueda M, Yoshikawa J. Coronary artery calcification revisited. *J Atheroscler Thromb* 13: 31–37, 2006. [PubMed: 16505589]

14. Farb A, Tang AL, Burke AP, Sessums L, Liang Y, Virmani R. Sudden coronary death. Frequency of active coronary lesions, inactive coronary lesions, and myocardial infarction. *Circulation* 92: 1701–1709, 1995. [PubMed: 7671351]

15. Fitzgerald PJ, Ports TA, Yock PG. Contribution of localized calcium deposits to dissection after angioplasty. An observational study using intravascular ultrasound. *Circulation* 86: 64–70, 1992. [PubMed: 1617791]

16. Hasegawa M, Watanabe Y. Rheological properties of the thoracic aorta in normal and WHHL rabbits. *Biorheology* 25: 147–156, 1988. [PubMed: 3196811]

17. Huang H, Virmani R, Younis H, Burke AP, Kamm RD, Lee RT. The impact of calcification on the biomechanical stability of atherosclerotic plaques. *Circulation* 103: 1051–1056, 2001. [PubMed: 11222465]

18. Humphrey JD *Cardiovascular Solid Mechanics: Cells, Tissues and Organs.* New York: Springer-Verlag, 2002.

19. Imoto K, Hiro T, Fujii T, Murashige A, Fukumoto Y, Hashimoto G, Okamura T, Yamada J, Mori K, Matsuzaki M. Longitudinal structural determinants of atherosclerotic plaque vulnerability: a computational analysis of stress distribution using vessel models and three-dimensional intravascular ultrasound imaging. *J Am Coll Cardiol* 46: 1507–1515, 2005. [PubMed: 16226176]

20. Jain A, Demer LL, Raizner AE, Hartley CJ, Lewis JM, Roberts R. In vivo assessment of vascular dilatation during percutaneous transluminal coronary angioplasty. *Am J Cardiol* 60: 988–992, 1987. [PubMed: 2960231]

21. Kolodgie FD, Gold HK, Burke AP, Fowler DR, Kruth HS, Weber DK, Farb A, Guerrero LJ, Hayase M, Kutys R, Narula J, Finn AV, Virmani R. Intraplaque hemorrhage and progression of coronary atheroma. *N Engl J Med* 349: 2316–2325, 2003. [PubMed: 14668457]

22. Li ZY, Howarth S, Tang T, Graves M, U-King-Im J, Gillard JH. Does calcium deposition play a role in the stability of atheroma? Location may be the key. *Cerebrovasc Dis* 24: 452–459, 2007. [PubMed: 17878727]

23. Loree HM, Kamm RD, Stringfellow RG, Lee RT. Effects of fibrous cap thickness on peak circumferential stress in model atherosclerotic vessels. *Circ Res* 71: 850–858, 1992. [PubMed: 1516158]

24. Luo G, Ducy P, McKee MD, Pinero GJ, Loyer E, Behringer RR, Karsenty G. Spontaneous calcification of arteries and cartilage in mice lacking matrix GLA protein. *Nature* 386: 78–81, 1997. [PubMed: 9052783]

25. Mal AK, Singh SJ. *Deformation of Elastic Solids.* Englewood Cliffs, NJ: Prentice-Hall, 1991.

26. Park JC, Siegel RJ, Demer LL. Effect of calcification and formalin fixation on in vitro distensibility of human femoral arteries. *Am Heart J* 125: 344–349, 1993. [PubMed: 8427126]

27. Pynadath TI, Mukherjee DP. Dynamic mechanical properties of atherosclerotic aorta. A correlation between the cholesterol ester content and the viscoelastic properties of atherosclerotic aorta. *Atherosclerosis* 26: 311–318, 1977. [PubMed: 849376]

28. Raggi P, Callister TQ, Cooil B, He ZX, Lippolis NJ, Russo DJ, Zelinger A, Mahmarian JJ. Identification of patients at increased risk of first unheralded acute myocardial infarction by electron-beam computed tomography. *Circulation* 101: 850–855, 2000. [PubMed: 10694523]

29. Richardson PD, Davies MJ, Born GV. Influence of plaque configuration and stress distribution on fissuring of coronary atherosclerotic plaques. *Lancet* 2: 941–944, 1989. [PubMed: 2571862]

30. Sherebrin MH, Bernans HA, Roach MR. Extensibility changes of calcified soft tissue strips from human aorta. *Can J Physiol Pharmacol* 65: 1878–1883, 1987. [PubMed: 3690406]

31. Tang D, Yang C, Kobayashi S, Ku DN. Effect of a lipid pool on stress/strain distributions in stenotic arteries: 3-D fluid-structure interactions (FSI) models. *J Biomech Eng* 126: 363–370, 2004. [PubMed: 15341174]

32. Tang D, Yang C, Zheng J, Woodard PK, Saffitz JE, Petruccelli JD, Sicard GA, Yuan C. Local maximal stress hypothesis and computational plaque vulnerability index for atherosclerotic plaque assessment. *Ann Biomed Eng* 33: 1789–1801, 2005. [PMCID: PMC1474005] [PubMed: 16389527]

33. Tintut Y, Parhami F, Bostrom K, Jackson SM, Demer LL. cAMP stimulates osteoblast-like differentiation of calcifying vascular cells. Potential signaling pathway for vascular calcification. *J Biol Chem* 273: 7547–7553, 1998. [PubMed: 9516456]

34. Ugural AC, Fenster SK. *Advanced Strength and Applied Elasticity.* Upper Saddle River, NJ: Prentice-Hall, 1995.

35. Vengrenyuk Y, Carlier S, Xanthos S, Cardoso L, Ganatos P, Virmani R, Einav S, Gilchrist L, Weinbaum S. A hypothesis for vulnerable plaque rupture due to stress-induced debonding around cellular microcalcifications in thin fibrous caps. *Proc Natl Acad Sci USA* 103: 14678–14683, 2006. [PMCID: PMC1595411] [PubMed: 17003118]

36. Wilkinson FL, Liu Y, Rucka AK, Jeziorska M, Hoyland JA, Heagerty AM, Canfield AE, Alexander MY. Contribution of VCAF-positive cells to neovascularization and calcification in atherosclerotic plaque development. *J Pathol* 211: 362–369, 2007. [PMCID: PMC1868967] [PubMed: 17154367]

37. Williamson SD, Lam Y, Younis HF, Huang H, Patel S, Kaazempur-Mofrad MR, Kamm RD. On the sensitivity of wall stresses in diseased arteries to variable material properties. *J Biomech Eng* 125: 147–155, 2003. [PubMed: 12661209]

Figures and Tables

Fig. 1.

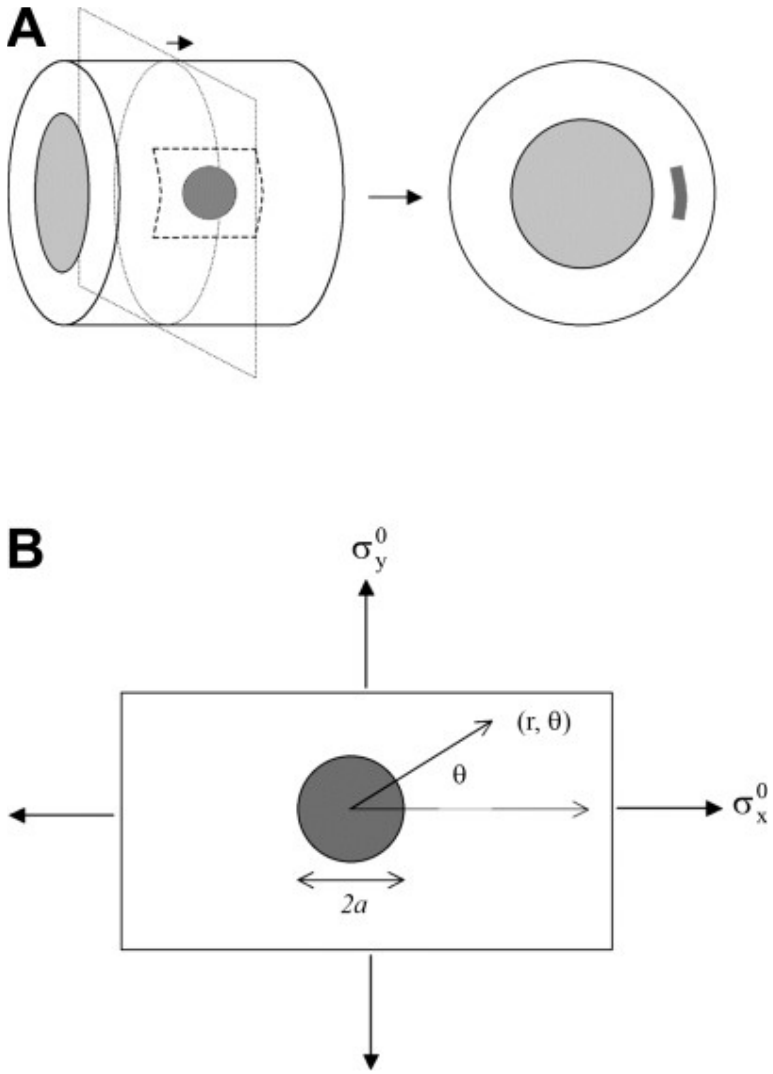

Schematic diagram of the hypothetical model used to assess mechanical stress around a calcium deposit in a distensible vessel. *A*: the cylinder (*left*) represents a model vascular segment. The shaded circle represents a calcium deposit, simplified to a thin circular disc. The dashed square represents the region evaluated for mechanical stress, including both vessel and deposit. A cross-sectional view is shown on the *right*. The shaded pattern on the *right* corresponds with the dashed square on the *left*. *B*: the rectangle corresponds with the shaded square in *A*. Polar coordinates (r, θ), diameter of the deposit ($2a$), and orientation of stresses (σ_y^o} and σ_x^o) are indicated.

Fig. 2.

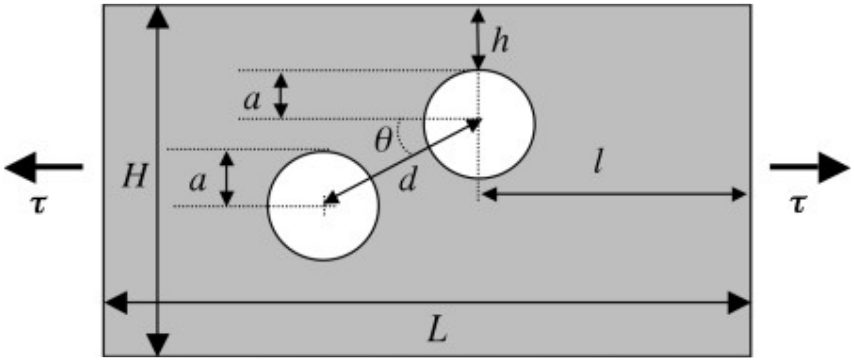

Schematic of finite element model. All parameters were varied over a specified range (some results not shown); values from the simulations presented in Fig. 5 are as follows: the inclusion diameter, a = 0.3 mm; the distance of the soft (lipidic) inclusion to the lumen, h = 0.05 mm; the distance between inclusions, d = 0.36 mm; height and width of the entire model, H = 1 mm and L = 1.95 mm; and the applied tension, τ = 10 kPa.

Fig. 3.

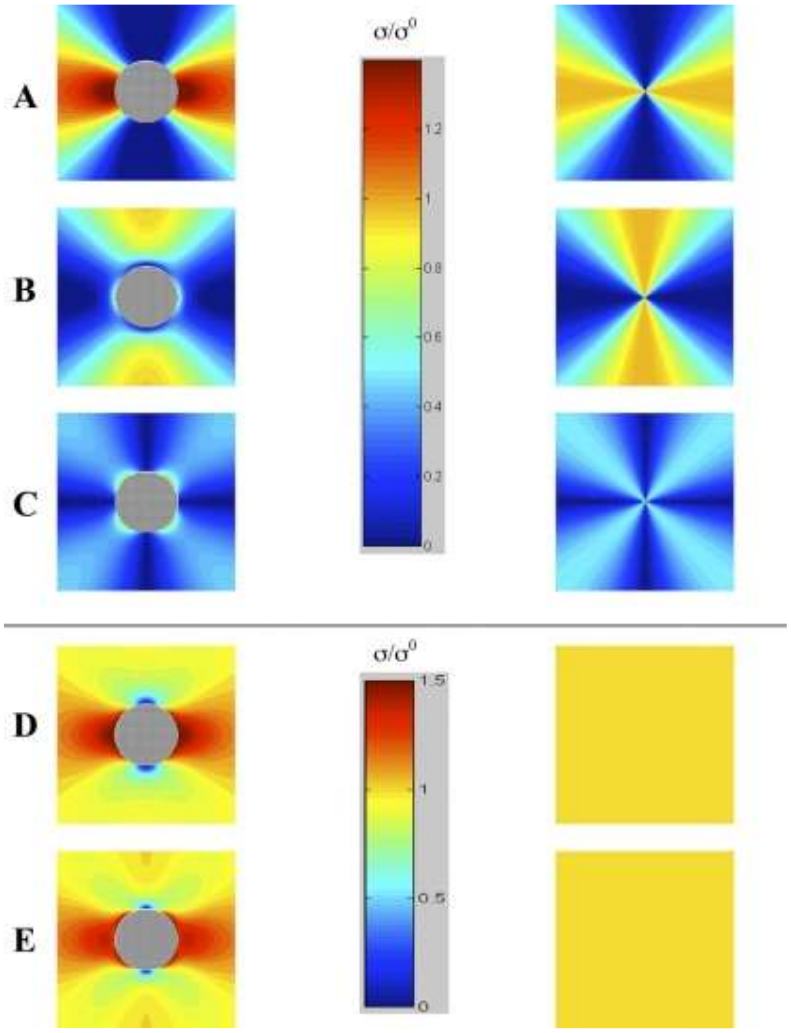

Stress distribution for uniaxial loading of distensible material with (*left*) and without (*right*) a rigid inclusion. Radial (*A*), circumferential (*B*), shear (*C*), normalized maximum principal (*D*), and von Mises (*E*) stresses. Vertical bars are pseudocolor scales for stress σ, normalized to the applied stress σ_0 in *A*–*C* and separately for stress in *D* and *E* (ν = 0.45).

Fig. 4.

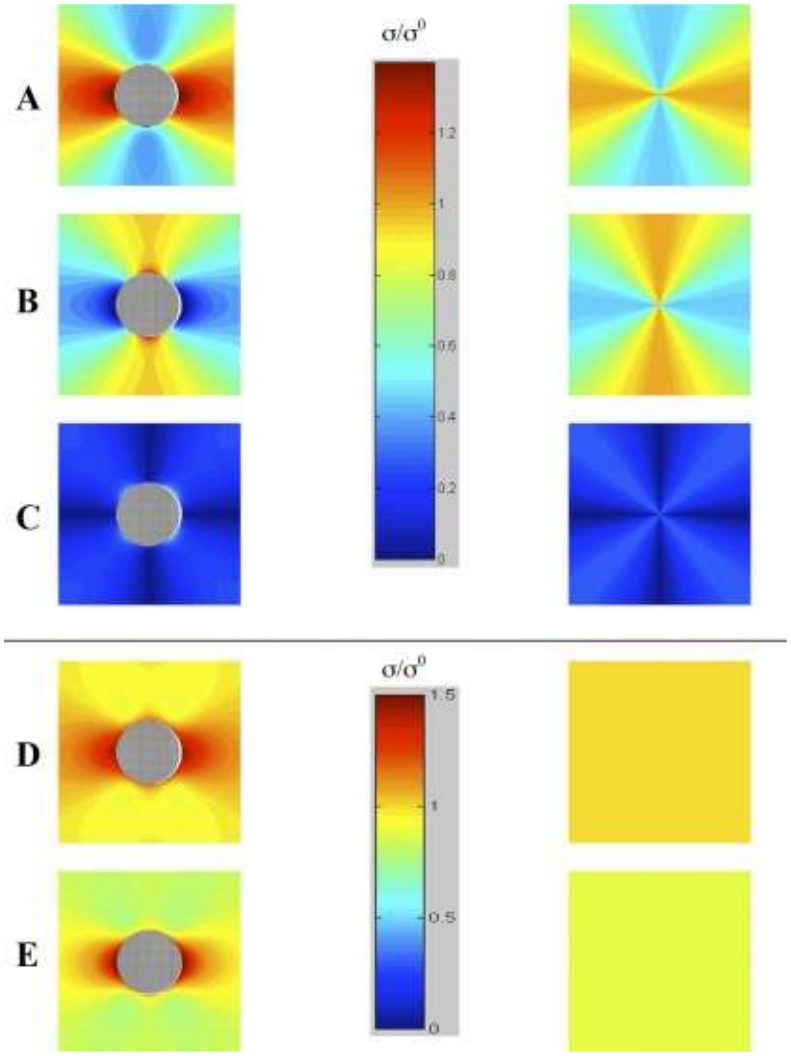

Stress distribution for biaxial loading of distensible material with a rigid inclusion (*left*) and without (*right*). Radial (*A*), circumferential (*B*), shear (*C*), normalized maximum principal (*D*), and von Mises (*E*) stresses. Vertical bars are pseudocolor scales for stress σ, normalized to the applied stress σ_0 in *A*–*C* and separately for stress in *D* and *E* (ν = 0.45).

Fig. 5.

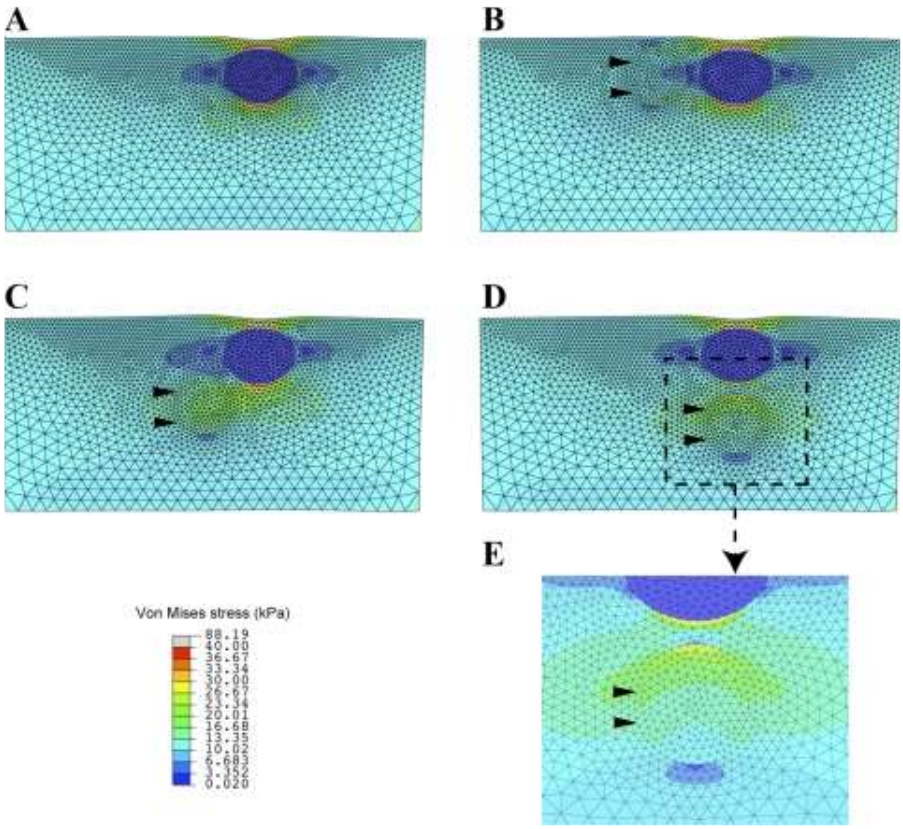

Von Mises stress distributions computed by finite element analysis. A uniform tension load of τ = 10 kPa was applied to the left and right edges to model the circumferential stress in the arterial wall, and the resulting deformation and stress states were computed by using the hyperelastic constitutive model described in the text. *A*: with only a soft (lipidic) inclusion and no stiff (calcific) inclusion. *B*: soft inclusion with neighboring stiff inclusion (arrowheads) equidistant from the lumen (θ = 0°). *C*: soft inclusion with stiff inclusion to one side and at greater distance from the lumen (θ = 45°). *D*: stiff inclusion abluminal to the soft inclusion (θ = 90°). *E*: magnified view of *D* focusing on a region of nominally high stress.

Fig. 6.

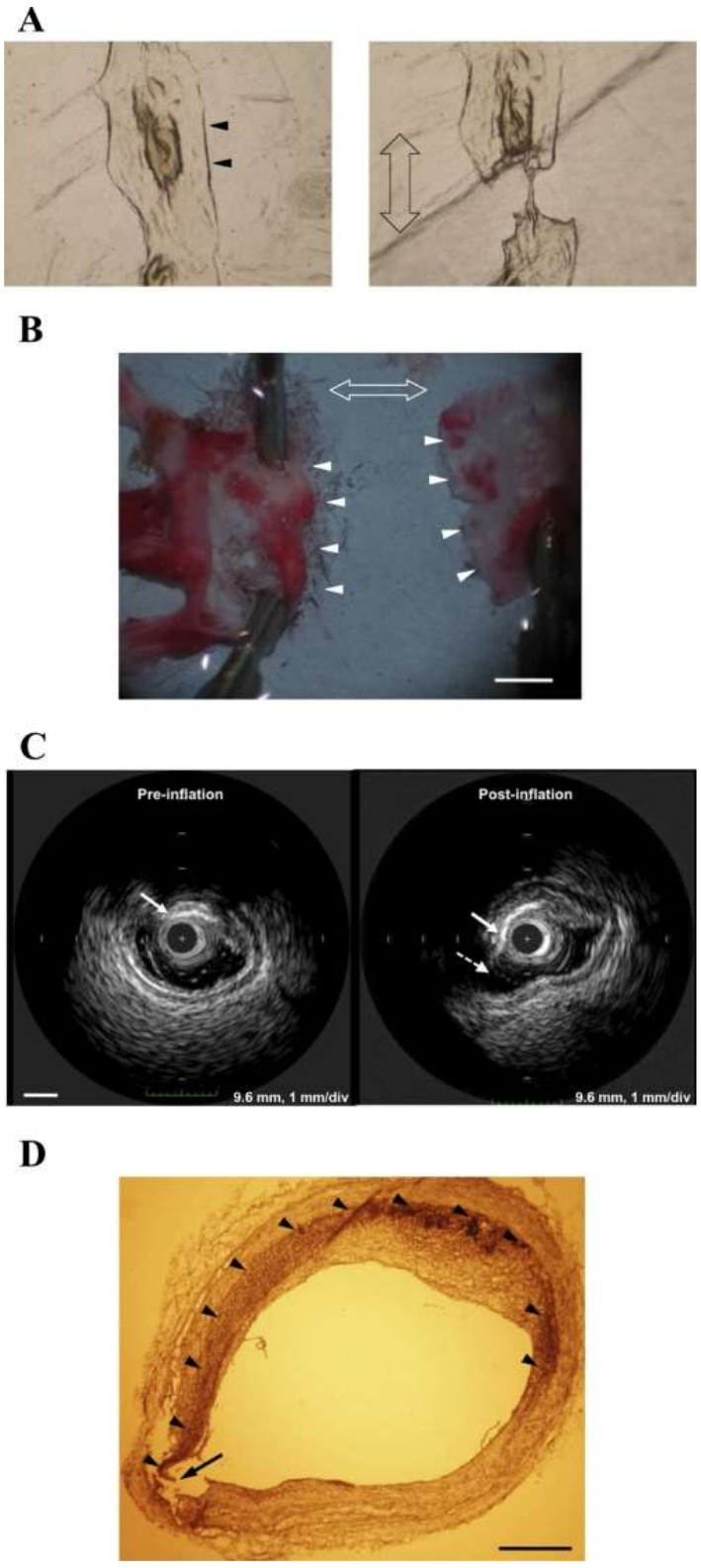

Biological models. *A*: in vitro model showing failure at the edge of a calcified nodule in a culture of calcifying vascular cells, containing mineralized nodules on a lawn of monolayer cells and extracellular matrix. Representative example of 3 cultures tested. Double-headed arrow indicates stress loading axis. Arrowheads indicate the calcified nodule, and distance between arrowheads is ~2 mm. *B*: ex vitro model showing failure at the edge of a calcified lesion in the Oil Red O stained ascending aorta from a hyperlipidemic (high fat-fed *ldlr*$^{-/-}$) mouse following uniaxial loading. Representative example of 3 aortas tested. Double-headed arrow indicates stress loading axis. Great arteries and aortic arch (cephalad) are on the *left*. Arrowheads indicate torn edges. Scale bar = 1 mm.

C: intravascular ultrasound images of atherosclerotic calcification in a human coronary artery obtained before and after intraluminal balloon inflation. After balloon inflation, failure (dashed arrow) is seen at the edge of the calcium deposit (solid arrows). Scale bar = 1 mm. *D*: Von Kossa staining of calcified human coronary artery after intraluminal balloon inflation. A circumferential arc of calcification (arrowheads) is seen in the vessel wall, with failure (arrow) seen at the end of the calcified arc facing the direction of the applied stress where compliance mismatch would be expected. Scale bar = 0.5 mm.